



HAL
open science

Spin-driven evolution of asteroids' top-shapes at fast and slow spins seen from (101955) Bennu and (162173) Ryugu

Masatoshi Hirabayashi, Ryota Nakano, Eri Tatsumi, Kevin J. Walsh, Olivier S. Barnouin, Patrick Michel, Christine S. Hartzell, Daniel Britt, Seiji Sugita, Sei-Ichiro Watanabe, et al.

► **To cite this version:**

Masatoshi Hirabayashi, Ryota Nakano, Eri Tatsumi, Kevin J. Walsh, Olivier S. Barnouin, et al.. Spin-driven evolution of asteroids' top-shapes at fast and slow spins seen from (101955) Bennu and (162173) Ryugu. *Icarus*, 2020, 352, pp.113946. 10.1016/j.icarus.2020.113946 . hal-03084677

HAL Id: hal-03084677

<https://hal.science/hal-03084677>

Submitted on 21 Dec 2020

HAL is a multi-disciplinary open access archive for the deposit and dissemination of scientific research documents, whether they are published or not. The documents may come from teaching and research institutions in France or abroad, or from public or private research centers.

L'archive ouverte pluridisciplinaire **HAL**, est destinée au dépôt et à la diffusion de documents scientifiques de niveau recherche, publiés ou non, émanant des établissements d'enseignement et de recherche français ou étrangers, des laboratoires publics ou privés.

1 **Spin-driven evolution of asteroids' top-shapes at fast and slow spins seen from**
2 **(101955) Bennu and (162173) Ryugu**

3
4 ¹Masatoshi Hirabayashi, ¹Ryota Nakano, ^{2,3}Eri Tatsumi, ⁴Kevin J. Walsh, ⁵Olivier S. Barnouin,
5 ⁶Patrick Michel, ⁷Christine M. Hartzell, ⁸Daniel T. Britt, ³Seiji Sugita, ^{9,10}Sei-ichiro Watanabe,
6 ⁴William F. Bottke, ¹¹Daniel J. Scheeres, ¹²Ronald-Louis Ballouz, ³Yuichiro Cho, ³Tomokatsu
7 Morota, ¹²Ellen S. Howell, and ¹²Dante S. Lauretta.

8
9 ¹Auburn University, Auburn, AL, USA.

10 ²Instituto de Astrofísica de Canarias, Tenerife, Spain

11 ³University of Tokyo, Tokyo, Japan

12 ⁴Southwest Research Institute, Boulder, CO, USA

13 ⁵The Johns Hopkins University Applied Physics Laboratory, Laurel, MD, USA

14 ⁶Université Côte d'Azur, Observatoire de la Côte d'Azur, CNRS, Laboratoire Lagrange, Nice,
15 France

16 ⁷University of Maryland, College Park, MD, USA

17 ⁸University of Central Florida, Orlando, FL, USA

18 ⁹Nagoya University, Nagoya 464-8601, Japan

19 ¹⁰Institute of Space and Astronautical Science (ISAS), Japan Aerospace Exploration Agency
20 (JAXA), Kanagawa, Japan

21 ¹¹University of Colorado, Boulder, CO, USA

22 ¹²Lunar and Planetary Laboratory, University of Arizona, Tucson, AZ, USA.

23 **Abstract**

24 Proximity observations by OSIRIS-REx and Hayabusa2 provided clues on the shape evolution
25 processes of the target asteroids, (101955) Bennu and (162173) Ryugu. Their oblate shapes with
26 equatorial ridges, or the so-called top shapes, may have evolved due to their rotational conditions
27 at present and in the past. Different shape evolution scenarios were previously proposed; Bennu's
28 top shape may have been driven by surface processing, while Ryugu's may have been developed
29 due to large deformation. These two scenarios seem to be inconsistent. Here, we revisit the
30 structural analyses in earlier works and fill a gap to connect these explanations. We also apply a
31 semi-analytical technique for computing the cohesive strength distribution in a uniformly rotating
32 triaxial ellipsoid to characterize the global failure of top-shaped bodies. Assuming that the
33 structure is uniform, our semi-analytical approach describes the spatial variations in failed regions
34 at different spin periods; surface regions are the most sensitive at longer spin periods, while
35 interiors fail structurally at shorter spin periods. This finding suggests that the shape evolution of
36 a top shape may vary due to rotation and internal structure, which can explain the different
37 evolution scenarios of Bennu's and Ryugu's top shapes. We interpret our results as the indications
38 of top shapes' various evolution processes.

39 **Highlights**

- 40 • We reanalyzed results from FEM analyses for asteroids Bennu and Ryugu, the targets of the
41 ongoing small body sample return missions, OSIRIS-REx and Hayabusa2, respectively.
- 42 • We applied a semi-analytical approach to quantify how the failure modes of top shapes vary
43 with spin and confirmed that the results from this approach were consistent with those from
44 the FEM approaches.
- 45 • The results show that the rotationally driven evolution of top shapes may consist of two
46 deformation processes: surface processing at a longer spin period and internal failure at a
47 shorter spin period.

48 **Key Words**

49 Asteroids; Asteroids, rotation; Asteroids, surfaces; Near-Earth objects; Regolith

50 **1. Introduction**

51 Small asteroids are considered to be leftovers generated by re-accumulation of regolith after
52 catastrophic disruptions of their parent bodies [e.g., Bottke et al., 2005, 2015; Morbidelli et al.,
53 2009; Walsh, 2018; Michel et al., 2020]. Near-Earth asteroids (101955) Bennu, a B-type asteroid,
54 and (162173) Ryugu, a Cb-type asteroid, are the targets of the ongoing asteroid sample return
55 missions OSIRIS-REx [Lauretta et al., 2019] and Hayabusa2 [Watanabe et al., 2019], respectively.
56 The recent proximity observations in these missions have given the detailed physical properties of
57 the target asteroids. The unique features of Bennu and Ryugu include the oblate shapes with
58 equatorial ridges, the so-called top-shapes (Figure 1). Re-accumulation processes after
59 catastrophic disruptions may play a key role in the formation of top shapes and their precursor
60 shapes [Michel et al., 2020]. These shapes may have further evolved into the complete form of top
61 shapes at later stages. The circularities of Bennu's and Ryugu's ridges (while the level of such
62 features may differ) suggest that their fast rotation at present or in the past may have contributed
63 to the current configurations of their top shapes. However, the evolution scenarios of their top
64 shapes have been proposed differently.

65 Bennu's equivalent radius was reported to be 245 m [Barnouin et al., 2019], which is
66 consistent with that estimated by radar observations, 246 m [Nolan et al., 2013]. The spin period
67 was determined as 4.3 h [Nolan et al., 2019; Hergenrother et al., 2019]. The bulk density is 1.19
68 g/cm³ [Scheeres et al., 2019], consistent with an earlier prediction by analyses of the Yarkovsky
69 drift [Chesley et al., 2014]. This low bulk density, as well as the observed thick regolith layers,
70 implies that Bennu is likely to be a rubble pile [Barnouin et al., 2019; Lauretta et al., 2019; Scheeres
71 et al., 2019; Walsh et al., 2019]. The variation in the surface slope is distinctive at lower and higher
72 latitudes, the boundary of which can be characterized by the size of the Roche lobe at the current
73 spin period [Scheeres et al., 2019]. This feature implies that the surface at lower latitudes is within
74 the Roche lobe and may have evolved due to materials from higher latitudes at present [Scheeres
75 et al., 2016, 2019]. Preliminary observations of the surface morphology found mass movements at
76 multiple scales [Walsh et al., 2019], which may have led to the present boulder distributions
77 [Lauretta et al., 2019] and the surface morphology like small and large grooves [Barnouin et al.,
78 2019]. Such surface diversities imply internal rigidity at low level in the body [Barnouin et al.,
79 2019]. Also, a plastic finite element model (FEM) approach showed that Bennu may not have
80 internal failure but may experience surface failure at the present spin period if the cohesive strength
81 is less than ~0.5 Pa [Scheeres et al., 2019].

84 Ryugu is a top-shaped asteroid with an equivalent radius of 500 m and is currently rotating
85 at a spin period of 7.6 h [Watanabe et al., 2019]. Ryugu’s bulk density is similar to Bennu’s, i.e.,
86 1.19 g/cm^3 [Watanabe et al., 2019], which implies that this asteroid is also a rubble pile. Observed
87 OH-bearing materials (but at low level) [Kitazato et al., 2019] and highly porous boulders with
88 low thermal inertia [Okada et al., 2020] imply that Ryugu may be a remnant after catastrophic
89 disruption of an undifferentiated parent body. Also, the Small Carry-on Impact experiment showed
90 that the artificial crater formation is in the gravity regime, implying that the surface is covered by
91 mechanically weak layers [Arakawa et al., 2020]. Unlike Bennu, however, Ryugu’s slope does not
92 reflect the current rotational condition. The slope variation becomes the smallest when the rotation
93 period is 3.5 h – 3.75 h. This finding led to an interpretation that there may have been reshaping
94 processes at this spin period. It was found that the surface morphology is less cratered in the
95 western region than that in the eastern region (the east-west dichotomy) [Sugita et al., 2019]. The
96 boulder distribution was also observed to be heterogeneous [Michikami et al., 2019], while mass
97 movements may be limited and correlate with the gravitational potential [Sugita et al., 2019].
98 Based on these observations, assuming that Ryugu’s structure is uniform, Hirabayashi et al. [2019]
99 hypothesized that large deformation occurred at a spin period of 3.5 – 3.75 h to produce the east-
100 west dichotomy.

101 These studies give some discrepancy of Bennu’s and Ryugu’s reshaping processes while
102 they have top shapes with a similar bulk density. Specifically, these two bodies are considered to
103 have been affected by rotationally driven deformation but may have evolved differently. Bennu’s
104 top shape may have evolved due to surface processing at present. The equatorial ridge may be
105 developed due to mass wasting on the surface while the interior is intact (no mass flows occur in
106 the interior). On the other hand, Ryugu’s shape may result from large deformation, perhaps caused
107 by internal failure. The interior becomes the most sensitive to structural failure at high spin, leading
108 to internal mass flows (inward flows along the spin axis and outward flows in the radial direction)
109 that make the shape oblate and push materials on the equatorial plane outward.

110 We fill a gap between these hypothesized reshaping processes. We revisit the FEM results
111 from earlier studies [Hirabayashi et al., 2019; Scheeres et al., 2019; Watanabe et al., 2019] and
112 explore the variations in the structural failure mode of these objects at different spin periods. To
113 support our discussion, we newly employ a semi-analytical approach proposed by Nakano et al.
114 [2020], who extended an approach by Hirabayashi [2015]. This semi-analytical approach
115 computes Bennu’s and Ryugu’s yield conditions by assuming their shapes to be uniformly rotating
116 triaxial ellipsoids and characterizes their global failure modes. We finally acknowledge Cheng et
117 al. [2020], who recently proposed that top-shaped asteroids like Ryugu and Bennu result from
118 mass movements in shallow surface layers at a fast rotation period. They assumed a large, rigid
119 core in a target sphere to reproduce a top shape. In the present study, the semi-analytical approach
120 and the FEM approach discuss the variations in the structural failure modes under the uniform
121 structure condition.

122 We outline the present manuscript. Section 2 briefly reviews the proposed evolution
123 processes of top-shaped asteroids. Section 3 shows the analysis approaches employed in this
124 manuscript: the plastic FEM approach and the semi-analytical approach. Section 4 summarizes the
125 results from our analyses. The results from the FEM approach are already introduced in
126 Hirabayashi et al. [2019], Scheeres et al. [2019], and Watanabe et al. [2019], and we compare these
127 results in this manuscript. Section 5 discusses the evolution of top-shaped asteroids based on the
128 results from Section 4. Our FEM approach assumes the structure of a body to be uniform. On the
129 other hand, the semi-analytical approach provides the distribution of the minimum cohesive

130 strength that can avoid structure failure (see the definition in Section 3) and give insights into the
131 dependence of the failure mode on the internal structure.

132

133 **2. Rotational evolution of top-shaped asteroids**

134 While Section 1 summarized the rotational evolution of top-shaped bodies by focusing on Bennu
135 and Ryugu, this section reviews the general background of such objects. Ground-based radar
136 observations show that spheroidal shapes are dominant in observed objects [e.g., Taylor et al.,
137 2012; Benner et al., 2015]. Among them are reported to be top shapes, some of which also have
138 smaller satellites [e.g., Ostro et al., 2006; Brozović et al., 2011; Becker et al., 2015; Busch et al.,
139 2011; Naidu et al., 2015, 2020; Walsh and Jacobson, 2015]. Some top shapes are rotating close to
140 their spin limits at which surface materials may be about to be shed [Scheeres et al., 2006; Harris
141 et al., 2009], while others like Ryugu are not [Watanabe et al., 2019]. Findings of top shapes in
142 different taxonomy types imply that the evolution of top shapes are not linked to the material
143 compositions of asteroids [e.g., Walsh et al., 2018]. After the formation of top shapes and their
144 precursor bodies during re-accumulation after catastrophic disruption [Michel et al., 2020], these
145 bodies may have evolved by experiencing fast rotation. There are two competing scenarios for
146 rotationally driven reshaping processes that may have induced top shapes.

147 First, surface processing may be the primary contributor to developing top shapes [e.g.,
148 Harris et al., 2009; Minton, 2008; Scheeres, 2015; Walsh et al., 2008, 2012; Cheng et al., 2020].
149 When the centrifugal force becomes dominant at fast rotation, surface mass movements may occur
150 towards lower potential regions around the equator, while the interior is intact [e.g., Sánchez and
151 Scheeres, 2018, 2020]. The equatorial ridge evolves by the accumulation of surface materials from
152 middle and high latitude regions. When materials slide down to the equatorial region, they may
153 experience the Coriolis force and move toward the longitudinal direction [Harris et al., 2009;
154 Statler et al., 2014]. Also, when surface processing is significant, the contacts of particles may tend
155 to induce more mass ejection on irregular surfaces [Yu et al., 2018].

156 Second, if the stress field in the interior is considered, another top-shape evolution process
157 may be possible [Hirabayashi and Scheeres, 2015]. With fast rotation, they should have higher
158 stress condition around the center of mass [Hirabayashi, 2015]. This mechanism results from force
159 vectors acting on each element that is affected by gravity and rotation. In a top shape, the direction
160 of the gravity force is radially inward, while that of the centrifugal force is horizontally outward.
161 When the body is rotating at fast spin, the centrifugal force at lower latitudes exceeds the gravity
162 force, leading to a horizontal, outward loading. At higher latitudes, on the other hand, the inward
163 component of the gravitational force is always dominant. These loading modes induce outward
164 deformation in the horizontal direction around the equator and inward deformation in the vertical
165 direction near the spin axis, possibly enhancing the evolution process of a top shape.

166 A stand-alone explanation of each scenario sounds incomplete to discuss the top-shape
167 evolution mechanism. If surface processing is a main driver that develops top shapes at fast spin,
168 the interior should be mechanically stronger than the surface layers. On the other hand, if the
169 mechanical strength of the interior is similar to that of the surface layer, the stress field in the
170 interior should reach its yield condition before surface regions experience mass movements
171 [Hirabayashi, 2015; Hirabayashi et al., 2015]. Gravity measurements implied that Ryugu's
172 structure may be homogeneous [Watanabe et al., 2019]. The present study attempts to explain the
173 correlation of surface and internal failure by considering the structural conditions at different spin
174 periods.

175

176 3. Analysis approach

177 3.1. Results from the earlier plastic FEM approach

178 A plastic FEM approach was developed and designed to analyze the locations of structurally failed
179 regions in an irregularly shaped body that is uniformly rotating. The developed code was
180 compatible with ANSYS Mechanical APDL 18.1. In this study, instead of conducting new FEM
181 analyses, we revisit the structural analysis results for Benu and Ryugu from our earlier works
182 [Watanabe et al., 2019; Scheeres et al., 2019; Hirabayashi et al., 2019]. We show how Benu and
183 Ryugu experience rotationally driven failure modes at multiple spin periods when the structure is
184 assumed to be uniform. While the present work does not provide new simulations, we briefly
185 introduce our FEM simulation settings below. Note that the detailed model development is also
186 provided in the earlier work [e.g., Hirabayashi et al., 2016; Hirabayashi and Scheeres, 2019].

187 The FEM meshes of Benu and Ryugu were generated from the mission-derived
188 polyhedron shape models [Barnouin et al., 2019; Watanabe et al., 2019]. We first used TetGen [Si,
189 2015] to convert polyhedron shape models to 4-node triangular FEM meshes. Then, these FEM
190 meshes were modified to obtain 10-node meshes. Because the meshes developed by TetGen were
191 not optimally compatible with the simulation environment in ANSYS, we refined them by
192 performing manual operations and by using the ANSYS mesh refining functions. The derived
193 mesh was further processed to provide the constraints on the spatial movements of nodes. To
194 mimic the condition of an irregularly shaped body in space, we gave constraints on three degree
195 of freedom at the center of gravity for the translational motion and another three degrees of
196 freedom at two surface nodes for the rotational motion [Hirabayashi and Scheeres, 2019]. We
197 computed a force loading acting on each node by accounting for the self-gravity force and the
198 centrifugal force.

199 Our model assumes that structural deformation is small and follows linear elasticity below
200 the yield condition and perfect plasticity on that condition. Perfect plasticity specifies that there is
201 no material hardening and softening. To define the yield condition, we used the Drucker-Prager
202 yield criterion, which is written as [Chen and Han, 1988]

$$204 \quad f = \alpha I_1 + \sqrt{J_2} - s \leq 0. \quad (1)$$

206 I_1 and J_2 are the stress invariants, which are given as

$$208 \quad I_1 = \sigma_1 + \sigma_2 + \sigma_3, \quad (2)$$

$$209 \quad J_2 = \frac{1}{6} \{(\sigma_1 - \sigma_2)^2 + (\sigma_2 - \sigma_3)^2 + (\sigma_3 - \sigma_1)^2\}, \quad (3)$$

210 where $\sigma_i (i = 1, 2, 3)$ is the principal stress component. α and s are material constants that are
212 defined as

$$214 \quad \alpha = \frac{2 \sin \phi}{\sqrt{3}(3 - \sin \phi)}, \quad s = \frac{6Y \cos \phi}{\sqrt{3}(3 - \sin \phi)}, \quad (4)$$

215 where ϕ and Y are the angle of friction and the cohesive strength, respectively. We note that Y is
217 defined in the sense of continuum media, which is the cumulative effect of cohesion caused by
218 grain-grain interactions in a given small element.

219 In our FEM simulations, the structural condition was assumed to be uniform over the entire
 220 body. Young’s modulus (E_s), Poisson’s ratio (μ), and the angle of friction (ϕ) were fixed at
 221 1×10^7 Pa, 0.25, and 35° , respectively [e.g., Lambe and Whitman, 1969]. For simplicity, no
 222 dilatancy was allowed in these simulations. The necessary parameters for FEM simulations are
 223 available in Table 1. To determine the structural failure mode of an irregularly shaped body at a
 224 given spin period, we changed the cohesive strength under the constant parameters. If the actual
 225 cohesive strength is enough to resist failure, the body can keep the original shape. However, as the
 226 cohesive strength becomes smaller, some regions in the body start failing structurally. We
 227 computed the distribution of failure and the minimum cohesive strength that the body can avoid
 228 failure anywhere (later denoted as Y^*) [Hirabayashi and Scheeres, 2019].
 229

230 **Table 1. Physical parameter settings in simulations. The dimensions are from Barnouin et al.**
 231 **[2019] for Bennu and Watanabe et al. [2019] for Ryugu.**

Physical Parameters	Symbols	Value	Units
Young’s modulus	E_s	1×10^7	[Pa]
Poisson’s ratio	ν	0.25	[-]
Angle of friction	ϕ	35	[deg]
Bulk density	ρ	1.19	[g/cm ³]
Bennu’s dimension	[$2a, 2b, 2c$]	$506 \times 492 \times 457$	[m ³]
Ryugu’s dimension	[$2a, 2b, 2c$]	$1,004 \times 1,004 \times 876$	[m ³]

232
 233 **3.2. Semi-analytical stress model**

234 While our plastic FEM approach can describe the failure modes of irregularly shaped bodies, the
 235 results of structural failure depend on local topographic features [Hirabayashi and Scheeres, 2019].
 236 Such local features may be too detailed to study global conditions that induce either surface
 237 processing or internal failure. Here, to characterize the mechanisms of such global failure modes,
 238 we apply a semi-analytical approach that computes the variations in the stress distributions in a
 239 uniformly rotating triaxial ellipsoid at different spin periods. Note that the model assumption of a
 240 rotating triaxial ellipsoid gives a reasonable approximation for the global failure modes of a top-
 241 shaped asteroid. The present approach is an extension of the previous approach, which focused on
 242 a spherical body [Hirabayashi, 2015]. This approach is first discussed by Nakano and Hirabayashi
 243 [2020].

244 The semi-analytical approach consists of two aspects. The first aspect is to compute the
 245 stress distribution in a uniformly triaxial ellipsoid by assuming linear elasticity [Dobrovolskis,
 246 1982; Holsapple, 2001; Love, 2011]. The second aspect is to use this stress distribution and the
 247 Drucker-Prager yield criterion to derive the minimum cohesive strength, Y_e^* , at given elements.
 248 We distinguish Y_e^* with Y^* , which is given as the minimum cohesive strength that a considered
 249 body starts to experience failure somewhere (from Section 3.1). Importantly, we define the
 250 following relationship: $Y^* = \max(Y_e^*)$. This approach does not provide the deformation processes
 251 but shows the sensitivity of a body element to structural failure. We confirmed that the earlier
 252 semi-analytical approach and the FEM approach gave consistent results for the failure modes of a
 253 uniformly rotating spherical body [Hirabayashi, 2015]. Below, we describe how to compute Y_e^* .
 254 The details are also found in Nakano and Hirabayashi [2020].

255 For the first aspect, the stress distribution in a uniformly rotating triaxial ellipsoid is
 256 computed based on linear elasticity [Dobrovolskis, 1982; Holsapple, 2001; Love, 2011].
 257 Considering the equilibrium state of stress, we can write the stress distribution as

258

259

$$\frac{\partial \sigma_{11}}{\partial x_1} + \frac{\partial \sigma_{12}}{\partial x_2} + \frac{\partial \sigma_{13}}{\partial x_3} + \rho b_1 = 0, \quad (5)$$

260

$$\frac{\partial \sigma_{21}}{\partial x_1} + \frac{\partial \sigma_{22}}{\partial x_2} + \frac{\partial \sigma_{23}}{\partial x_3} + \rho b_2 = 0, \quad (6)$$

261

$$\frac{\partial \sigma_{31}}{\partial x_1} + \frac{\partial \sigma_{32}}{\partial x_2} + \frac{\partial \sigma_{33}}{\partial x_3} + \rho b_3 = 0, \quad (7)$$

262

263 where σ_{ij} ($i, j = 1, 2, 3$) is the stress component, ρ is the bulk density, which is assumed to be
 264 uniform over the entire volume, and b_i ($i = 1, 2, 3$) is the body force, which includes a centrifugal
 265 force and a self-gravity force [Holsapple, 2001]. In these equations, $\sigma_{12} = \sigma_{21}$, $\sigma_{32} = \sigma_{23}$, and
 266 $\sigma_{13} = \sigma_{31}$. Because a triaxial ellipsoid is axisymmetric, we define the x_1 , x_2 , and x_3 axes along
 267 the minimum, intermediate, and maximum moment of inertia axes, respectively.

268

269

270

From Equations (5) through (7), the displacement u_i in the x_i direction is expressed with
 12 parameters [Dobrovolskis, 1982],

271

$$u_1 = x_1 \left[A + B \frac{x_1^2}{a^2} + C \frac{x_2^2}{b^2} + D \frac{x_3^2}{c^2} \right], \quad (8)$$

272

$$u_2 = x_2 \left[E + F \frac{x_1^2}{a^2} + G \frac{x_2^2}{b^2} + H \frac{x_3^2}{c^2} \right], \quad (9)$$

273

$$u_3 = x_3 \left[I + J \frac{x_1^2}{a^2} + K \frac{x_2^2}{b^2} + L \frac{x_3^2}{c^2} \right], \quad (10)$$

274

275 where a , b , and c are the semi-major axis, the semi-intermediate axis, and the semi-minor axis,
 276 respectively ($a \geq b \geq c$). Also, the upper alphabets indicate coefficients that are determined by
 277 the constitutive law and the boundary condition. Using Equations (8) through (10), we can describe
 278 the strain components as

279

280

$$\epsilon_{ij} = \frac{1}{2} \left(\frac{\partial u_i}{\partial x_j} + \frac{\partial u_j}{\partial x_i} \right). \quad (11)$$

281

282

We next consider Hooke's law (linear elasticity), which is given as

283

284

$$\sigma_{ij} = \lambda \epsilon_{kk} \delta_{ij} + 2\mu \epsilon_{ij}, \quad (12)$$

285

286 where $\epsilon_{kk} = \epsilon_{11} + \epsilon_{22} + \epsilon_{33}$ and δ_{ij} is the Kronecker delta. λ and μ are Lamé's constants, which
 287 are given as

288

289

$$\lambda = \frac{E_s \nu}{(1 + \nu)(1 - 2\nu)}, \quad (13)$$

290

$$\mu = \frac{E_s}{2(1 + \nu)}. \quad (14)$$

291

292

The traction boundary condition is given as

293
294
$$\sigma_{ij}n_j = 0, \tag{15}$$

295
296 where n_j is written as

297
298
$$n_1 = \frac{x_1}{a^2\chi}, n_2 = \frac{x_2}{b^2\chi}, n_3 = \frac{x_3}{c^2\chi}, \tag{16}$$

299
300 and

301
$$\chi = \left(\frac{x_1^2}{a^4} + \frac{x_2^2}{b^4} + \frac{x_3^2}{c^4} \right)^{\frac{1}{2}}. \tag{17}$$

302
303 Combining all these conditions, we obtain 12 linear equations to uniquely determine the 12
304 coefficients appearing in Equations (8) through (10).

305 For the second aspect, we convert these stress components to the principal stress
306 components, σ_1 , σ_2 , and σ_3 . Then, we substitute these principal components into Equation (1).
307 Using the constant parameters defined in Table 1, we compute the distribution of Y_e^* in a uniformly
308 triaxial ellipsoid at different spin periods. Specifically, Y_e^* is computed by considering $f = 0$ in
309 Equation (1).

310
311 **4. Comparison of the structural conditions between Bennu and Ryugu**

312 **4.1. Results from finite element analysis approach**

313 We first summarize the failure modes of Bennu and Ryugu at different spin periods by introducing
314 the earlier results from our plastic FEM approach [Hirabayashi et al., 2019; Scheeres et al., 2019;
315 Watanabe et al., 2019]. The present study shows the dependence of the failure mode on the spin
316 period, which was also predicted for irregularly shaped bodies by Hirabayashi and Scheeres [2019].
317 If Bennu and Ryugu are rotating at longer spin periods, their failure mode is characterized as
318 surface failure. On the other hand, if they are rotating at shorter spin periods, internal failure
319 becomes significant. We describe the contrasts of these processes by referring to the plastic FEM
320 results [Hirabayashi et al., 2019; Scheeres et al., 2019; Watanabe et al., 2019].

321 Figure 2 shows the failure modes of Bennu at spin periods of 4.3 h (the current spin period)
322 and 3.5 h [Scheeres et al., 2019]. At the 4.3 h spin period, the interior does not fail structurally,
323 while the surface regions at middle and high latitudes are sensitive to structural failure (Panels a
324 and b). This failure mode appears when the cohesive strength is ~ 0.2 Pa. If the cohesive strength
325 of surface materials is below this level, mass movements should occur. The flow processes
326 observed by OSIRIS-REx [Barnouin et al., 2019; Scheeres et al., 2016, 2019; Walsh et al., 2019;
327 Jawin et al., 2020] imply that tin top-layers may be covered with cohesionless materials. Thus, our
328 results support that Bennu's top shape may have evolved by surface processing at the present spin
329 period. At the 3.5 h spin period, on the other hand, Bennu should experience internal failure if the
330 cohesion is less than 0.8 Pa. The central region is the most sensitive to structural failure; the
331 predicted failed region is almost axisymmetric and reaches the top surface.

332 Ryugu's structural behavior is similar to Bennu's, although the variations in the failed
333 regions appear due to local topography at some level (Figure 3). At a spin period of 7.6 h (the
334 current spin period), the structure does not reach the yield condition in the almost entire volume
335 when the cohesive strength is fixed at 1 Pa (Panels a and b). This trend results from self-gravity,

336 which leads the interior to have compression with limited shear and thus not to experience
337 structural failure significantly. At a spin period of 3.5 h, internal failure becomes significant
338 [Watanabe et al., 2019]. Unlike the symmetric failed region appeared in Bennu at the 3.5 h spin
339 period, Ryugu’s failed region is asymmetric (Panels c and d) [Hirabayashi et al., 2019]. Structural
340 failure is observed to be more concentrated in the central area and in the bottom-right part of the
341 plots. This asymmetric distribution of the failed region may imply that in the current shape,
342 Ryugu’s internal structure at the 3.5 h spin period is divided into a structurally relaxed region (the
343 upper-left part) and an unrelaxed region (the bottom-right part).

344 From these structural conditions at different spin periods, the evolution process of Ryugu’s
345 top shape was interpreted to be different from that of Bennu’s. Ryugu’s top shape may have
346 evolved by large deformation when this asteroid was rotating at a spin period of 3.5 ~ 3.75 h
347 [Watanabe et al., 2019]. Because of Ryugu’s east-west dichotomy, the surface in the western
348 region is smoother than that in the eastern region [Sugita et al., 2019]. Also, the equatorial ridge
349 in the western region is sharper than that in the eastern region [Watanabe et al., 2019]. The
350 locations of the failed regions predicted from the plastic FEM approach correspond to those of the
351 eastern region [Hirabayashi et al., 2019]. Therefore, the relatively less cratered condition of the
352 western region implies that this region may be structurally relaxed due to a large deformation
353 process at a spin period of 3.5 h ~ 3.75 h [Hirabayashi et al., 2019]. We note that when Ryugu’s
354 spin has slowed down to the current spin period, 7.6 h, the body may have also had surface
355 processing as Bennu has.

356

357 **4.2. Results from semi-analytical approach**

358 The FEM approach gave a significant interpretation that Bennu’s top shape may result from
359 surface processing at the current spin period, 4.3 h, while Ryugu’s may be developed by large
360 deformation, which is due to internal failure, at a spin period of 3.5 h ~ 3.75 h. This contrast
361 between Bennu’s and Ryugu’s failure modes implies that top shapes may be able to evolve by both
362 surface processing and internal deformation. This section uses the semi-analytical approach, which
363 can describe global failure modes, to further explore how these failure modes appear at different
364 spin periods. We compute the distribution of Y_e^* over slices of Bennu and Ryugu along their spin
365 axis. We incorporate the parameter conditions defined in Table 1 into the semi-analytical model.

366 First, we discuss the distribution of Y_e^* for Bennu in Figure 4. We observe that the
367 distribution of Y_e^* varies as a function of the spin period. When the spin period is shorter than 3.5
368 h, Y_e^* becomes the maximum at the center of the body. At a spin period of 3 h, for example, Y_e^* at
369 the central region reaches higher than 12 Pa. Y_e^* on the surface in the equatorial region is lower
370 than that in the central region, but still higher than 0 Pa. In the polar regions, Y_e^* becomes 0 Pa,
371 implying that there is no strength necessary to avoid structural failure. This result indicates that
372 the interior is the most sensitive to structural failure if the actual cohesive strength is uniform over
373 the body. At a spin period longer than 3.75 h, nonzero Y_e^* is concentrated in the equatorial surface
374 region but does not appear in the central region. As the spin period continues to become longer,
375 the regions with nonzero Y_e^* become smaller. At a spin period of 4.3 h (the current spin period),
376 nonzero Y_e^* only appears in shallow surface regions at the equator. In this region, Y_e^* is less than 1
377 Pa. This result indicates that if the actual cohesive strength is less than that level, surface materials
378 should slide down to regions at lower latitudes. This interpretation is consistent with what was
379 observed from the plastic FEM approach (Figure 2).

380 Next, we show the distribution of Y_e^* for Ryugu. The bulk density of Ryugu is the same as
381 that of Bennu. Their global shapes are also similar. Therefore, we anticipate that Ryugu’s failure

382 mode is similar to Bennu's. Figure 5 illustrates the failure modes of Ryugu at spin periods from
383 2.5 h to 7.6 h. The magnitude of Y_e^* for Ryugu is higher than that for Bennu because of the size
384 difference. At a spin period shorter than 3.5 h, the region around the center needs higher Y_e^* to
385 resist structural failure. However, when the spin period is around 3.75 h, the region with nonzero
386 Y_e^* is separated towards the equatorial surface regions. As the spin period becomes longer, this
387 region shrinks and eventually disappears. At a spin period of 7.6 h, there is no obvious region with
388 nonzero Y_e^* . This result implies that there is no significant deformation at the current spin period.
389 Again, the results are consistent with those from the plastic FEM approach (Figure 3).

390 Our semi-analytical model describes that if the structure is uniform, structural failure in
391 Ryugu and Bennu can be characterized by two modes. The first mode is that the interior
392 structurally fails first at fast spin. This mode can induce vertical compression along the spin axis
393 and radial deformation in the horizontal direction. The second mode is that surface processing is
394 dominant, and top-surface layers at low and middle latitudes fail structurally at low spin. For these
395 failure modes, the size of internal failure is larger than that of surface failure. As the spin period
396 becomes longer, the transition occurs when nonzero Y^* disappears from the central region and is
397 split towards the surface regions. While these modes are apparently different, they induce mass
398 movements towards the equatorial region and thus can generate top shapes. The similar finding
399 was presented by Hirabayashi [2015] for a limited case in which a body is perfectly spherical.

400

401 **5. Discussion**

402 **5.1. Surface processing and internal deformation can develop a top-shaped body**

403 The results in Section 4 showed that both surface processes and internal deformation can contribute
404 to the evolution of Bennu's and Ryugu's top shapes. At a longer rotation period, surface layers are
405 the most sensitive to structural failure, while an interior is structurally intact. If surface layers do
406 not have enough cohesive strength, they should be modified. As the spin period becomes shorter,
407 the area of elements sensitive to structural failure increases. Eventually, the central region becomes
408 the most sensitive. At this stage, the interior fails structurally, leading to a deformation mode that
409 consists of a horizontal, outward flow and a vertical, inward flow. The development of a top shape
410 due to these two processes was confirmed by studies that used Discrete Element Model [e.g.,
411 Hirabayashi et al., 2015; Sánchez and Scheeres, 2016, 2018, 2020; Walsh et al., 2008, 2012; Yu
412 et al., 2020; Zhang et al., 2017, 2018].

413 The dependence of deformation on the spin period controls the evolution of a top shape.
414 Because the centrifugal force is the main contributor to reshaping, the shape evolves so that its
415 moment of inertia along the spin axis always increases (Section 4). Because the angular momentum
416 is constant during such a deformation process, the spin period becomes longer. On the other hand,
417 YORP may accelerate/decelerate the spin state, depending on the shape and how these effects have
418 affected the body [e.g., Bottke et al., 2015; Statler, 2009, 2015]. If top shapes spin up, they again
419 become sensitive to another deformation process.

420 The magnitude of reshaping may be controlled by the evolution of the spin period. In Figure
421 6, we show the schematics of possible paths of the evolution process of a top shape. When the
422 body is spinning at a spin period at which internal failure occurs (the upper path), deformation is
423 large. This deformation process leads to a higher moment of inertia under constant angular
424 momentum, making the spin period longer. After this event, deformation stops. To have another
425 deformation process, the body needs to be rotationally accelerated for a long time. On the other
426 hand, if the body is spinning at relatively slow spin, surface processes can still occur (the lower
427 path), and the magnitude of deformation may be small. Because the rotational change may be small

428 during such an event, it is not necessary for the body to wait for a long spin-up duration to have
429 another small deformation event. This implies that surface processing events occur more
430 frequently than internal deformation. The paths can interact with each other. This evolution process
431 indicates a complex coupling relationship between the shape and the spin period evolution [Cotto-
432 Figueroa et al., 2015]. Also, we point out that deformation is not necessarily axisymmetric.
433 Structural and shape heterogeneity even at small level can induce asymmetric deformation
434 processes [Hirabayashi et al., 2015; Sánchez, 2015; Sánchez and Scheeres, 2016]. When a
435 structurally weak location experiences deformation, that region should be relaxed structurally.
436 Then, the body that had deformation in one area now has structural sensitivities in other areas,
437 which may deform later.

438 Benu has complex trends of mass movements [Walsh et al., 2019; Jawin et al., 2020] and
439 unique morphologies such as grooves [Barnouin et al., 2019]. The energy analysis showed that the
440 boundary of the Roche lobe at the current spin period would be consistent with the surface slope
441 variation observed [Scheeres et al., 2016, 2019]. These findings imply that Benu’s surface
442 topography is currently evolving. The present study implies that at the current spin period, Benu’s
443 interior should be structurally intact, while its surface is sensitive to structural failure (Figure 4).
444 By “intact”, we mean that Y_e^* in the interior is zero, thus deformation driven by rotation may not
445 occur. This condition leads to surface processing from the middle latitudes to the equatorial regions
446 if the strength is low. Each mass movement event is small and asymmetric. Because the change at
447 the spin period is small, deformation processes occur occasionally. Also, Benu’s not-perfectly-
448 circular equatorial ridge imply that the spin period has not reached 3.5 h, and the ridge has evolved
449 within the gravity force-dominant region, i.e. the inside of the Roche lobe. If Benu had
450 experienced a shorter spin period than 3.5 h, the ridge would have been modified to be circular
451 due to a strong centrifugal force [Scheeres et al., 2016, 2019].

452 Ryugu’s top shape, on the other hand, may have evolved due to large deformation. This
453 idea was supported by its almost-perfectly-circular equatorial ridge. Watanabe et al. [2019] pointed
454 out that such a circular ridge might indicate the centrifugal force-gravity force boundary that has
455 occurred at a critical spin period, 3.5 h. At this spin period, the interior of this asteroid becomes
456 the most sensitive to structural failure (Section 4). Hayabusa2 showed that the western region looks
457 apparently younger than the eastern region [Sugita et al., 2019]. This east-west dichotomy implies
458 different time scales for the reshaping process [Hirabayashi et al., 2019]. First, a large-scaled
459 deformation may have occurred to create the global feature of Ryugu’s top shape (such as its
460 equatorial ridge). Then, another large-scaled deformation may have happened in the western
461 region and developed its young, smooth terrain.

462 From these analyses, we conclude that both internal deformation and surface processing
463 can lead to top shapes. After re-accumulation processes due to catastrophic disruptions [Michel et
464 al., 2020], precursor bodies experience these processes at different spin periods in complex ways
465 to evolve into top shapes. Again, it was previously argued that top shapes would be attributed to
466 one of these processes only.

467
468 **5.2. Insights into reshaping and top shapes’ interiors from surface morphologies**
469 While the present study assumed that the structure of Ryugu and Benu are homogeneous, small
470 bodies may have local heterogeneity at some level, given their formation and evolution processes.
471 Many bodies smaller than 100 km in diameter may result from the collisional evolution of larger
472 bodies [Bottke et al., 2005, 2015; Morbidelli et al., 2009; Walsh, 2018]. The following re-
473 accumulation processes may cause the heterogeneities of rubble pile asteroids [Michel et al., 2020].

474 Even after re-accumulation, deformation processes can change their volumes, changing the density
475 distribution [e.g., Hirabayashi and Scheeres, 2015; Scheeres et al., 2019; Bagatin et al., 2020].
476 Granular convections may modify the structure of asteroids [e.g., Murdoch et al., 2013; Yamada
477 and Katsuragi, 2014]. Seismic shaking may be a driver that induces granular convection. We note
478 that seismic waves may be significantly attenuated in granular media in a microgravity
479 environment [Yasui et al., 2015; Matsue et al., 2020], as seen by the Hayabusa2 SCI impact
480 experiment [Arakawa et al., 2020, Nishiyama et al., 2020]. Hypervelocity impact processes also
481 resurface and reorganize the interior, depending on their energy levels [e.g., Wünnemann et al.,
482 2006].

483 The failure mode of a top-shaped asteroid depends on such structural heterogeneities
484 [Hirabayashi, 2015]. Based on the distributions of Y_e^* in Ryugu and Bennu (Figures 4 and 5),
485 Figure 7 describes the dependence of the failure mode on the cohesive strength. This schematic
486 was first introduced by Hirabayashi [2015]; in the present study, we also add the case of a weak
487 interior proposed by Sánchez and Scheeres [2018]. If the structure is uniform, both surface
488 processing and internal failure can contribute to reshaping. When structurally weaker layers are
489 placed on top of a stronger interior, only surface particles can move at high spin [Hirabayashi et
490 al., 2015; Sánchez and Scheeres, 2016, 2018, 2020; Yu et al., 2020]. If the interior is weaker than
491 the surface layer, complex reshaping may occur to generate irregularly shaped bodies rather than
492 top shapes [Sánchez and Scheeres, 2018].

493 The observed crater morphologies may imply local heterogeneity of Bennu and Ryugu. On
494 Bennu, some small craters exhibit the discontinuities of the boulder size distribution inside and
495 outside the rims [Walsh et al., 2019]. Similar features are also observed on Ryugu [Sugita et al.,
496 2019; Watanabe et al., 2020; Morota et al., 2020]. Small particles are distributed inside such craters,
497 while the outside exhibits larger boulders [Walsh et al., 2019]. One explanation may be grain
498 segregation due to granular convection such as the Brazil nut effect [Watanabe et al., 2020].
499 Another explanation may be that small particles move on top surface layers more favorably than
500 large boulders and are depleted [Szalay et al., 2018]. If this is the case, top surface layers can be
501 considered to be mechanically weak and have evolved rapidly. Such transportation may be driven
502 not only by combinations of the centrifugal force and the gravitational force but also by other
503 mechanisms. An example may be electrostatic lofting, the amount of which is dependent on
504 cohesion and large electrostatic forces driven by photoemission or secondary electron emission
505 [Hartzell, 2019; Hartzell et al., 2020; Wang et al., 2016; Zimmerman et al., 2016]. Micrometeoroid
506 impacts [e.g., Sugita et al., 2019; Walsh et al., 2019] and thermal cracking [e.g., Moralo et al.,
507 2015, 2017; Hazeli et al., 2018] may also result in small particle transportation.

508

509 **5.3. Necessary technical improvements**

510 We finally discuss that the current study has two issues that need to be solved in our future work.
511 First, our discussions assumed that the body has a uniform structure. However, as discussed in
512 Section 5.2, there may exist some structural heterogeneity. If this is the case, we expect the
513 variations in the internal structure. Such variations affect our simulation settings, e.g., the friction
514 angle and the density distribution. Second, our model does not give detailed local failure modes,
515 which may highly correlate with the timescale that materials have been exposed to space
516 weathering. In carbonaceous asteroids, space weathering may make materials bluer and redder,
517 depending on their conditions [Gillis-Davis et al., 2017; Hendrix et al., 2019; Lantz et al., 2017;
518 Matsuoka et al., 2015; Thompson et al., 2019]. Recent studies pointed out that on both Bennu and
519 Ryugu, space weathering may redden materials [Sugita et al., 2019; Morota et al., 2020;

520 DellaGuistina et al., 2019, 2020] while space weathering on Bennu needs further interpretations.
521 However, the distribution of bluer materials is highly localized, and our models are too coarse to
522 provide consistent results. These issues need to be resolved to give stronger insights into the
523 evolution mechanisms of top-shaped asteroids.

524

525 **6. Conclusion**

526 The present study explored the rotationally driven evolution of Bennu's and Ryugu's top shapes.
527 We started by revisiting the previously reported results derived from a plastic FEM approach. The
528 semi-analytical approach was then introduced to describe the minimum cohesive strength
529 distribution that can avoid structural failure at a given element, under the assumption that a top
530 shape is a uniformly rotating triaxial ellipsoid. We then quantified how the failure modes of Bennu
531 and Ryugu would vary at different spin periods. The results showed that the failure modes
532 depended on the spin period. For these bodies, surface regions would be sensitive to structural
533 failure at a long spin period, while interiors could be the most vulnerable at a higher spin period.
534 Therefore, we suggest that top shapes can evolve by various reshaping processes that depend on
535 both rotation and internal structure.

536

537 **Acknowledgments**

538 M.H. and R.N. thank support from NASA/Solar System Workings
539 (NNH17ZDA001N/80NSSC19K0548) and Auburn University/Intramural Grant Program. Also,
540 the FEM results shown in this manuscript are obtained by using ANSYS Mechanical APDL 18.1.

541

542 **Reference**

543 Arakawa, M. et al. (2020), An artificial impact on the asteroid 162173 Ryugu formed a crater in
544 the gravity-dominated regime, Accepted in Science.

545

546 Bagatin, A. C. et al. (2020), Gravitational re-accumulation as the origin of most contact binaries
547 and other small body shapes, *Icarus*, 339, 113603, doi:10.1016/j.icarus.2019.113603.

548

549 Barnouin, O. S. et al. (2019), Shape of (101955) Bennu indicative of a rubble pile with internal
550 stiffness, *Nature Geosciences*, 12, p.247-252, doi:10.1038/s41561-019-0330-x.

551

552 Becker, T. M. et al. (2015), Physical modeling of triple near-Earth Asteroid (153591) 2001 SN263
553 from radar and optical light curve observations, *Icarus*, 248, p.499-515,
554 doi:10.1016/j.icarus.2014.10.048.

555

556 Benner, L. A. M. et al. (2015), Radar observations of near-Earth and main-belt asteroids. In
557 *Asteroid IV*, p.165 – 182, University of Arizona, Tucson, doi:10.2458/azu-
558 uapress_9780816532131-ch009.

559

560 Bottke, W. F. et al. (2005), Linking the collisional history of the main asteroid belt to its dynamical
561 excitation of depletion, *Icarus*, 179, 1, p.63-94, doi:10.1016/j.icarus.2005.05.017.

562

563 Bottke, W. F. et al. (2015), In search of the source of asteroid (101955) Bennu: Applications of
564 the stochastic YORP model, *Icarus*, 247, p.191 – 217, doi:10.1016/j.icarus.2014.09.046.

565

566 Brozović, M. et al. (2011), Radar and optical observations and physical modeling of triple near-
567 Earth Asteroid (136617) 1994 CC, *Icarus*, 216, 1, p.241-256, doi:10.1016/j.icarus.2011.09.002.
568

569 Busch, M. W. et al. (2011), Radar observations and the shape of near-Earth asteroid 2008 EV5,
570 *Icarus*, 212, 2, p.649-660, doi:10.1016/j.icarus.2011.01.013.
571

572 Chen and Han (2007), *Plasticity for structural engineers*, Springer-Verlag.
573

574 Cheng, B. et al. (2020), Surface boulders as clues for reconstructing the formation history of top-
575 shaped asteroids, *Nature Astronomy*, under review.
576

577 Chesley, S. R. et al. (2014), Orbit and bulk density of the OSIRIS-REx target asteroid (101955)
578 Bennu, *Icarus*, 235, p.5-22, doi:10.1016/j.icarus.2014.02.020.
579

580 Cotto-Figueroa, D. et al. (2015), Coupled spin and shape evolution of small rubble-pile asteroids:
581 self-limitation of the YORP effect, *The Astrophysical Journal*, 803, 1, 25, doi:10.1088/0004-
582 637X/803/1/25.
583

584 DellaGuistina, D. N. et al (2019), Properties of rubble-pile asteroid (101955) Bennu from OSIRIS-
585 REx imaging and thermal analysis, *Nature Astronomy*, 3, p.341 – 351, doi:10.1038/s41550-019-
586 0731-1.
587

588 DellaGuistina, D. N. et al. (2020), Reflectance and color heterogeneity on asteroid Bennu, 51st
589 Lunar and Planetary Science Conference, Houston, Texas, 2363.
590

591 Dobrovolskis, A. R. (1982), Internal stresses in phobos and other triaxial bodies, *Icarus*, 52, 1,
592 p.136 – 148, doi:10.1016/0019-1035(82)9017409.
593

594 Gillis-Davis, J. J. et al. (2017), Incremental laser space weathering of Allende reveals non-linear
595 like space weathering effects, *Icarus*, 286, p.1 - 14, doi:10.1016/j.icarus.2016.12.031.
596

597 Harris, A. W. et al. (2009), On the shapes and spins of “rubble pile” asteroids, *Icarus*, 199, p.310
598 – 318, doi:10.1016/j.icarus.2008.09.012
599

600 Hartzell, C. M. (2019), Dynamics of 2D electrostatic dust levitation at asteroids, *Icarus*, 333, p.234
601 – 242, doi:10.1016/j.icarus.2019.05.013.
602

603 Hartzell, C. M. et al. (2020), An Evaluation of Electrostatic Lofting as an Active Mechanism on
604 Bennu, *JGR: Planets*, Under Review.
605

606 Hazeli, K. et al. (2018), The origins of Asteroidal rock disaggregation: Interplay of thermal fatigue
607 and microstructure, *Icarus*, 304, p.172 – 182, doi:10.1016/j.icarus.2017.12.035.
608

609 Hendrix, A. R. and F. Vilas (2019), C-complex asteroids: UV-visible spectral characteristics and
610 implications for space weathering effects, *Geophysical Research Letters*, 46,
611 doi:10.1029/2019GL085883.

612
613 Hergenrother, C. W. et al. (2019), The operational environment and rotational acceleration of
614 asteroid (101955) Bennu from OSIRIS-REx observations, *Nature Communications*, 10, 1291,
615 doi:10.1038/s41467-019-09213-x.
616
617 Hirabayashi, M. and D. J. Scheeres (2015), Stress and Failure Analysis of Rapidly Rotating
618 Asteroid (29075) 1950 DA, *The Astrophysical Journal Letters*, 798, 1, L8, doi:10.1088/2041-
619 8205/798/1/L8.
620
621 Hirabayashi, M. et al. (2015), Internal Failure of Asteroids Having Surface Shedding due to
622 Rotational Instability, *The Astrophysical Journal*, 808, 63, doi:10.1088/0004-637X/808/1/63.
623
624 Hirabayashi, M. (2015), Failure modes and conditions of a cohesive, spherical body due to YORP
625 spin-up, *Monthly Notices of the Royal Astronomical Society*, 454, 2, p.2,249 – 2,257,
626 doi:10.1093/mnras/stv2017
627
628 Hirabayashi, M. et al. (2016), Fission and reconfiguration of bilobate comets as revealed by
629 67P/Churyumov-Gerasimenko, *Nature*, 534, p.352 – 355, doi:10.1038/nature17670.
630
631 Hirabayashi, M. and D. J. Scheeres (2019), Rotationally induced failure of irregularly shaped
632 asteroids, *Icarus*, 317, p.354 – 364, doi:10.1016/j.icarus.2018.08.003.
633
634 Hirabayashi, M. et al. (2019), The Western Bulge of 162173 Ryugu Formed as a Result of a
635 Rotationally Driven Deformation Process, *The Astrophysical Journal Letters*, 874, 1, L10,
636 doi:10.3847/2041-8213/ab0e8b.
637
638 Holsapple, K. A. (2001), Equilibrium Configurations of Solid Cohesionless Bodies, *Icarus*, 154,
639 2, p.432-448, doi:10.1006/icar.2001.6683.
640
641 Jawin, E. R. et al. (2020), The geology of (101955) Bennu from the first year of OSIRIS-REx
642 observations, 51th Lunar and Planetary Science Conference, Houston, Texas, 1201.
643
644 Kitazato, K. et al. (2019), The surface composition of asteroid 162173 Ryugu from Hayabusa2
645 near-infrared spectroscopy, *Science*, 364, 6,437, p.272 – 275, doi:10.1126/science.aav7432.
646
647 Lambe, T. W. and R. V. Whitman (1969), *Soil Mechanics*, John Wiley & Sons.
648
649 Lantz, C. et al. (2017), Ion irradiation of carbonaceous chondrites: A new view of space weathering
650 on primitive asteroids, *Icarus*, 285, p.43 - 57, doi:10.1016/j.icarus.2016.12.019.
651
652 Lauretta, D. S. et al. (2019), The unexpected surface of asteroid (101955) Bennu, *Nature*, 568, 55
653 – 66, doi:10.1038/s41586-019-1033-6.
654
655 Love, A. E. H. (2011), *A Treatise on the Mathematical Theory of Elasticity*, Dover, 4th Edition.
656

657 Matsue, K. et al. (2020), Measurements of seismic waves induced by high-velocity impacts:
658 Implications for seismic shaking surrounding impact craters on asteroids, *Icarus*, 338, 113520,
659 doi:10.1016/j.icarus.2019.113520.
660

661 Matsuoka, M. et al. (2015), Pulse-laser irradiation experiments of Murchison CM2 chondrite for
662 reproducing space weathering on C-type asteroids, *Icarus*, 254, p.135 - 143,
663 doi:10.1016/j.icarus.2015.02.029.
664

665 Michel, P. et al. (2020), Formation of top-shaped asteroids by collisional disruption: implications
666 for the origin of Ryugu and Bennu, *Nature Communications*, 11, 2,655, doi:10.1038/s41467-020-
667 16433-z.
668

669 Michikami, T. et al. (2019), Boulder size and shape distributions on asteroid Ryugu, *Icarus*, 331,
670 p.179 – 191, doi:10.1016/j.icarus.2019.05.019.
671

672 Minton, D. A. (2008), The topographic limits of gravitationally bound, rotating sand piles, *Icarus*,
673 195, 2, p.698 – 704, doi:10.1016/j.icarus.2008.02.009.
674

675 Molaro, J. L. et al. (2015), Grain-scale thermoelastic stresses and spatiotemporal temperature
676 gradients on airless bodies, implications for rock breakdown, *Journal of Geophysical Research*,
677 *Planets*, 120, p.255 – 277, doi:10.1002/2014JE004729.
678

679 Molaro, J. L. et al. (2017), Thermally induced stresses in boulders on airless body surfaces, and
680 implications for rock breakdown, *Icarus*, 294, p.247 – 261, doi:10.1016/j.icarus.2017.03.008.
681

682 Morbidelli, A. et al. (2009), Asteroids were born big, *Icarus*, 204, 2, p.558-573,
683 doi:10.1016/j.icarus.2009.07.011.
684

685 Morota, T. et al. (2020), Surface evolution of carbonaceous asteroid 162173 Ryugu revealed from
686 global mapping and touchdown operation of Hayabusa2, 368, 6,491, p.654-659,
687 doi:10.1126/science.aaz6306.
688

689 Murdoch, N. et al. (2013), Granular Convection in Microgravity, *Physical Review Letter*, 110,
690 029902, doi:10.1103/PhysRevLett.110.018307.
691

692 Naidu, S. P. et al. (2015), Radar imaging and characterization of the binary near-earth asteroid
693 (185851) 2000 DP107, *The Astronomical Journal*, 150, 54 (12pp), doi:10.1088/0004-
694 6256/150/2/54.
695

696 Naidu, S. P. et al. (2020), Radar observations and a physical model of binary near-Earth asteroid
697 65803 Didymos, target of the DART mission, *Icarus*, 348, 15, 113777,
698 doi:10.1016/j.icarus.2020.113777.
699

700 Nakano, R. and M. Hirabayashi (2020), Mass shedding activities of Asteroid (3200) Phaethon
701 enhanced by its rotation, Accepted in *The Astrophysical Journal Letters*.
702

703 Nishiyama, G. et al. (2020), An absence of seismic shaking on Ryugu induced by the impact
704 experiment on the Hayabusa2 mission, 51th Lunar and Planetary Science Conference, Houston,
705 Texas, 1806.
706

707 Nolan, M. C. et al. (2013), Shape model and surface properties of the OSIRIS-REx target Asteroid
708 (101955) Bennu from radar and lightcurve observations, *Icarus*, 226, 1, p.626-640,
709 doi:10.1016/j.icarus.2013.05.028.
710

711 Nolan, M. C. et al. (2019), Detection of Rotational Acceleration of Bennu Using HST Light Curve
712 Observations, *Geophysical Research Letters*, 46, p.1,956-1,962, doi:10.1029/2018GL/080658.
713

714 Okada, T. et al. (2020), Highly porous nature of a primitive asteroid revealed by thermal imaging,
715 *Nature*, Accepted in *Nature*.
716

717 Ostro, S. J. et al. (2006), Radar Imaging of Binary Near-Earth Asteroid (66391) 1999 KW4,
718 *Science*, 314, 5,803, p.1,276-1,280, doi:10.1126/science.1133622.
719

720 Sánchez, P. (2015), Asteroid Evolution: Role of Geotechnical Properties, *Asteroids: New*
721 *Observations, New Models Proceedings IAU Symposium*, 318, S. R. Chesley, A. Morbidelli, R.
722 Jedicke, and D. Farnocchia, eds, doi:10.1017/S1743921315008583.
723

724 Sánchez, P. and Scheeres, D. J. (2016), Disruption patterns of rotating self-gravitating aggregates:
725 A survey on angle of friction and tensile strength, *Icarus*, 271, p.453 – 471,
726 doi:10.1016/j.icarus.2016.01.016.
727

728 Sánchez, P. and D. J. Scheeres (2018), Rotational evolution of self-gravitating aggregates with
729 cores of variable strength, *Planetary and Space Science*, 157, p.39 – 47,
730 doi:10.1016/j.pss.2018.04.001.
731

732 Sánchez, P. and D. J. Scheeres (2020), Cohesive regolith on fast rotating asteroids, *Icarus*, 338,
733 113443, doi:10.1016/j.icarus.2019.113443.
734

735 Si, H. (2015), TetGen, a Delaunay-based Quality Tetrahedral mesh Generator, *ACM Transactions*
736 *on Mathematical Software (TOMS)*, 41, 2, 11, doi:10.1145/2629697.
737

738 Scheeres, D. J. et al. (2006), Dynamical Configuration of Binary Near-Earth Asteroid (66391)
739 1999 KW4, *Science*, 314, 5,803, p.1,280-1,283, doi:10.1126/science.1133599.
740

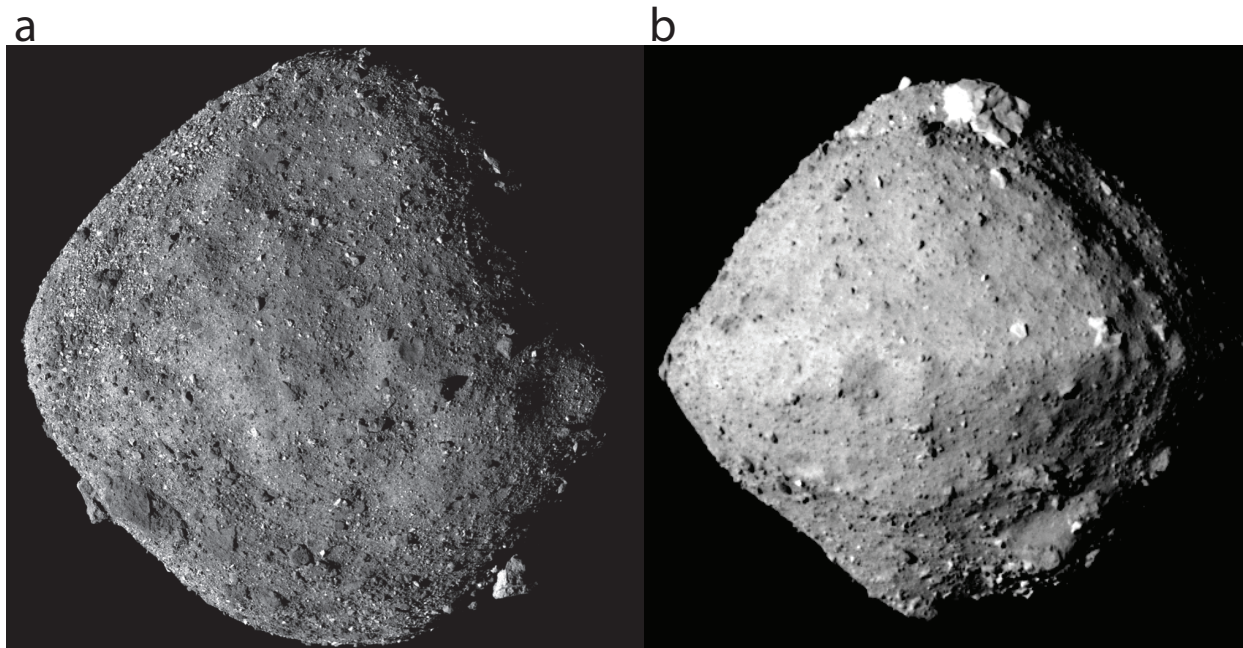
741 Scheeres, D. J. (2015), Landslides and Mass shedding on spinning spheroidal asteroids, *Icarus*,
742 247, p.1 – 17, doi:10.1016/j.icarus.2014.09.017.
743

744 Scheeres, D. J. et al. (2016), The geophysical environment of Bennu, *Icarus*, 276, p.116-140,
745 doi:10.1016/j.icarus.2016.04.013.
746

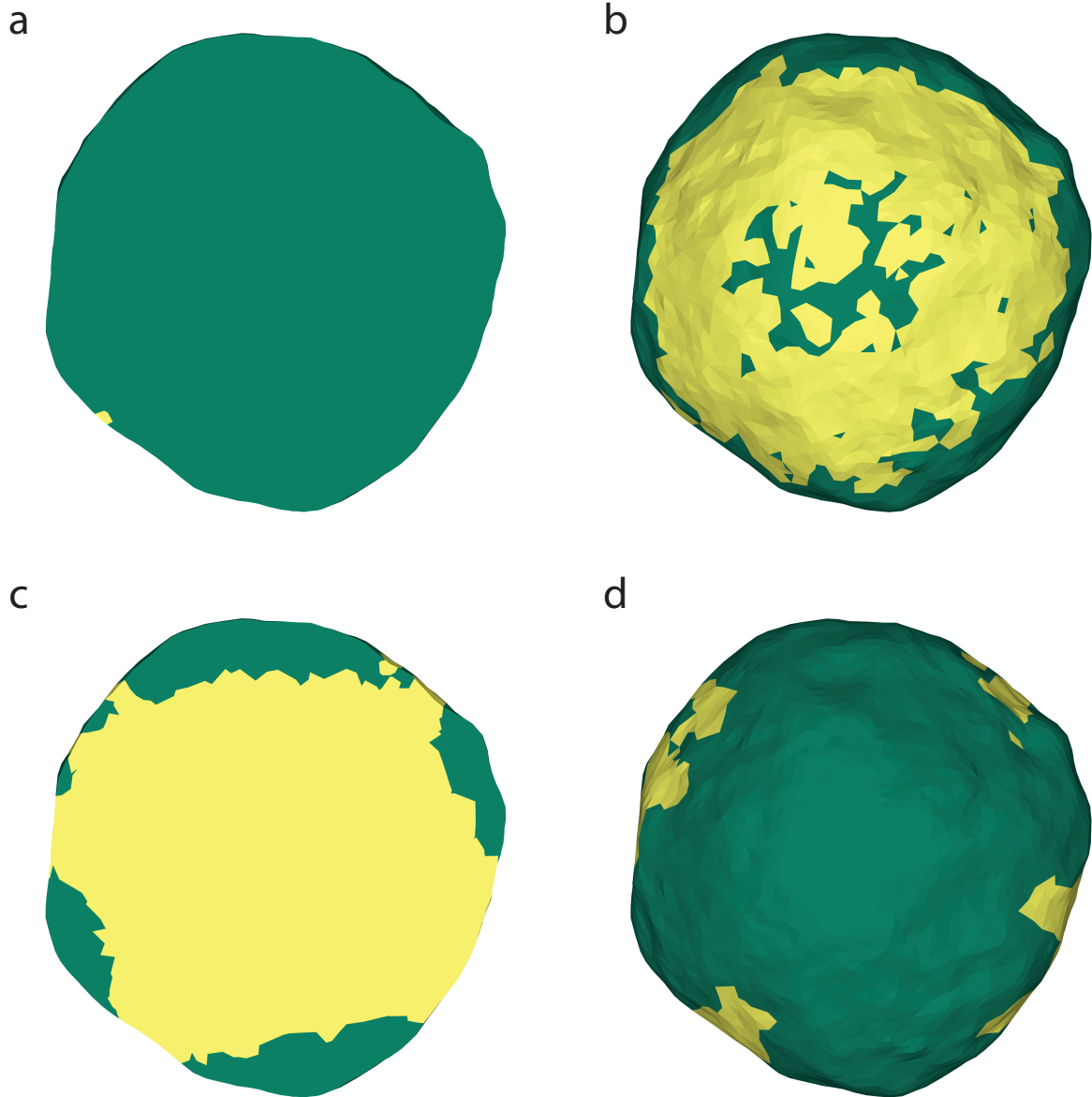
747 Scheeres, D. J. et al. (2019), The dynamic geophysical environment of (101955) Bennu based on
748 OSIRIS-REx measurements, *Nature Astronomy*, 3, p.352-361, doi:10.1038/s41550-019-0721-3.

749
750 Scheeres, D. J. et al. (2020), Higher-order gravity and global geophysical properties of (101955)
751 Bennu, 51th Lunar and Planetary Science Conference, Houston, Texas, 1786.
752
753 Statler, T. S. (2009), Extreme sensitivity of the YORP effect to small-scale topography, *Icarus*,
754 202, 2, p.502 – 513, doi:10.1016/j.icarus.2009.03.003.
755
756 Statler, T. (2014), Mechanism of self-reinforcing YORP acceleration for fast-rotating asteroids,
757 *Asteroids, Comets, Meteors 2014*, Proceedings of the conference held on 30 June – 4 July, 2014,
758 in Helsinki, Finland. Edited by Muinonen et al.
759
760 Statler, T. S. (2015), Obliquity of “top-shaped” asteroids may not imply reshaping by YORP spin-
761 up, *Icarus*, 248, p.313 – 317, doi:10.1016/j.icarus.2014.10.050.
762
763 Sugita, S. et al. (2019), The geomorphology, color, and thermal properties of Ryugu: Implications
764 for parent-body processes, *Science*, 364, 6,437, eaaw0422, doi:10.1126/science.aaw0422.
765
766 Szalay, J. R. et al. (2018), Dust Phenomena Relating to Airless Bodies, *Space Science Review*,
767 214, 98, doi:10.1007/s11214-018-0527-0
768
769 Thompson, M. S. et al. (2019), Spectral and chemical effects of simulated space weathering of
770 Murchison CM2 carbonaceous chondrite, *Icarus*, 319, p.499 - 511,
771 doi:10.1016/j.icarus.2018.09.022.
772
773 Walsh, K. J. et al. (2008), Rotational breakup as the origin of small binary asteroids, *Nature*, 454,
774 p.188 – 192, doi:10.1038/nature07078.
775
776 Walsh, K. J. et al. (2012), Spin-up of rubble-pile asteroids: Disruption, satellite formation, and
777 equilibrium shapes, *Icarus* 220, 2, p.514 – 529, doi:10.1016/j.icarus.2012.04.029.
778
779 Walsh, K. J. and S. A. Jacobson (2015), Formation and Evolution of Binary Asteroids, In *Asteroid*
780 *IV*, p.375 – 393, University of Arizona, Tucson, doi:10.2458/azu_uapress_9780816532131-ch20.
781
782 Walsh, K. J. (2018), Rubble Pile Asteroids, *Annual Review of Astronomy and Astrophysics*, 56,
783 p.593 – 624, doi:10.1146/annurev-astro-081817-052013.
784
785 Walsh, K. J. et al. (2019), Craters, boulders and regolith of (101955) Bennu indicative of an old
786 and dynamic surface, *Nature Geoscience*, 12, p.242 – 246, doi:10.1038/s41561-019-0326-6.
787
788 Wang, X. et al. (2016), Dust charging and transport on airless planetary bodies, *Geophysical*
789 *Research Letters*, 43, 12, p.6,103 – 6,110, doi:10.1002/2016GL069491.
790
791 Watanabe, S. et al. (2019), Hayabusa2 arrives at the carbonaceous asteroid 162173 Ryugu – A
792 spinning top-shaped rubble pile, *Science*, 364, 6,437, p.268-272, doi:10.1126/science.aav8032.
793

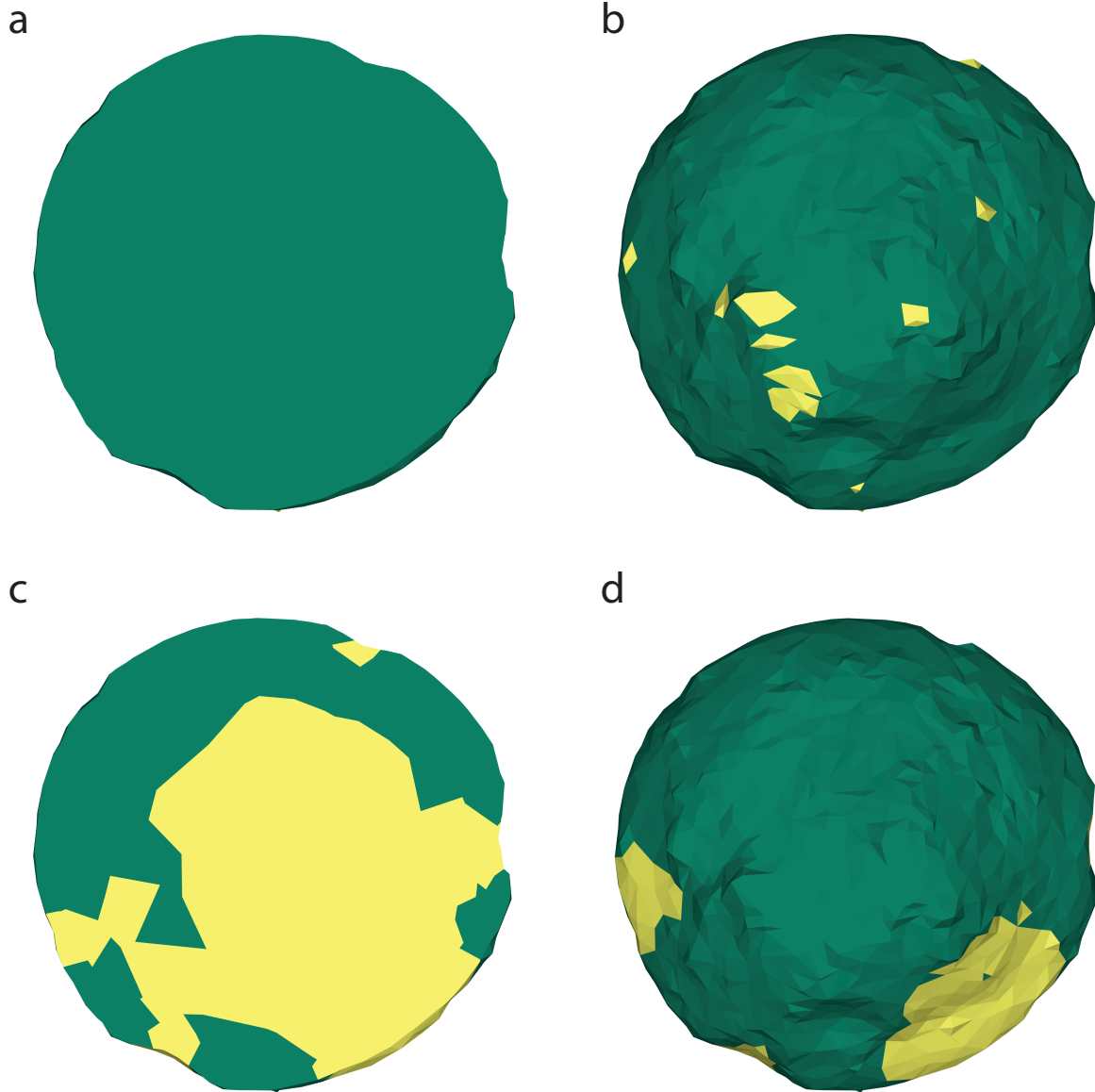
794 Watanabe, S. et al. (2020), Paucity of boulders in shallow craters on asteroid 162173 Ryugu, 51th
795 Lunar and Planetary Science Conference, Houston, Texas, 1675.
796
797 Wünnemann, K. et al. (2006), A strain-based porosity model for use in hydrocode simulations of
798 impacts and implications for transient crater growth in porous targets, *Icarus*, 180, p.514 – 527,
799 doi:10.1016/j.icarus.2005.10.013.
800
801 Yamada, T. M. and H. Katsuragi, Scaling of convective velocity in a vertically vibrated granular
802 bed, *Planetary and Space Science*, 100, p.79 – 86, doi:10.1016/j.pss.2014.05.019.
803
804 Yasui, M et al. (2015), Experimental study on impact-induced seismic wave propagation through
805 granular materials, *Icarus*, 260, p.320 – 331, doi:10.1016/j.icarus.2015.07.032.
806
807 Yu, Y. et al. (2018), The Dynamical Complexity of Surface Mass Shedding from a Top-shaped
808 Asteroid Near the Critical Spin Limit, *The Astronomical Journal*, 156, 59, doi:10.3847/1538-
809 3881/aacc7.
810
811 Zhang, Y. et al. (2017), Creep stability of the proposed AIDA mission target 65803 Didymos: I.
812 Discrete cohesionless granular physics model, *Icarus*, 294, p.98 – 123,
813 doi:10.1016/j.icarus.2017.04.027.
814
815 Zhang, Y. et al. (2018), Rotational Failure of Rubble-pile Bodies: Influences of Shear and
816 Cohesive Strength, *The Astrophysical Journal*, 857:15, doi:10.3847/1538-4357/aab5b2.
817
818 Zimmerman, M. I. et al. (2016), Grain-scale supercharging and breakdown on airless regoliths,
819 *Journal of Geophysical Research: Planets*, 121, p.2,150 – 2,165, doi:10.1002/2016JE005049.
820
821



824
825 **Figure 1. Images of Bennu (Panel a) and Ryugu (Panel b). Panel a. Image credit:**
826 **NASA/Goddard/University of Arizona. Panel b. Image credit: JAXA/UTokyo/Kochi U./Rikkyo**
827 **U./Nagoya U./Chiba Ins. Tech/Meiji U./U. Aizu/AIST.**
828

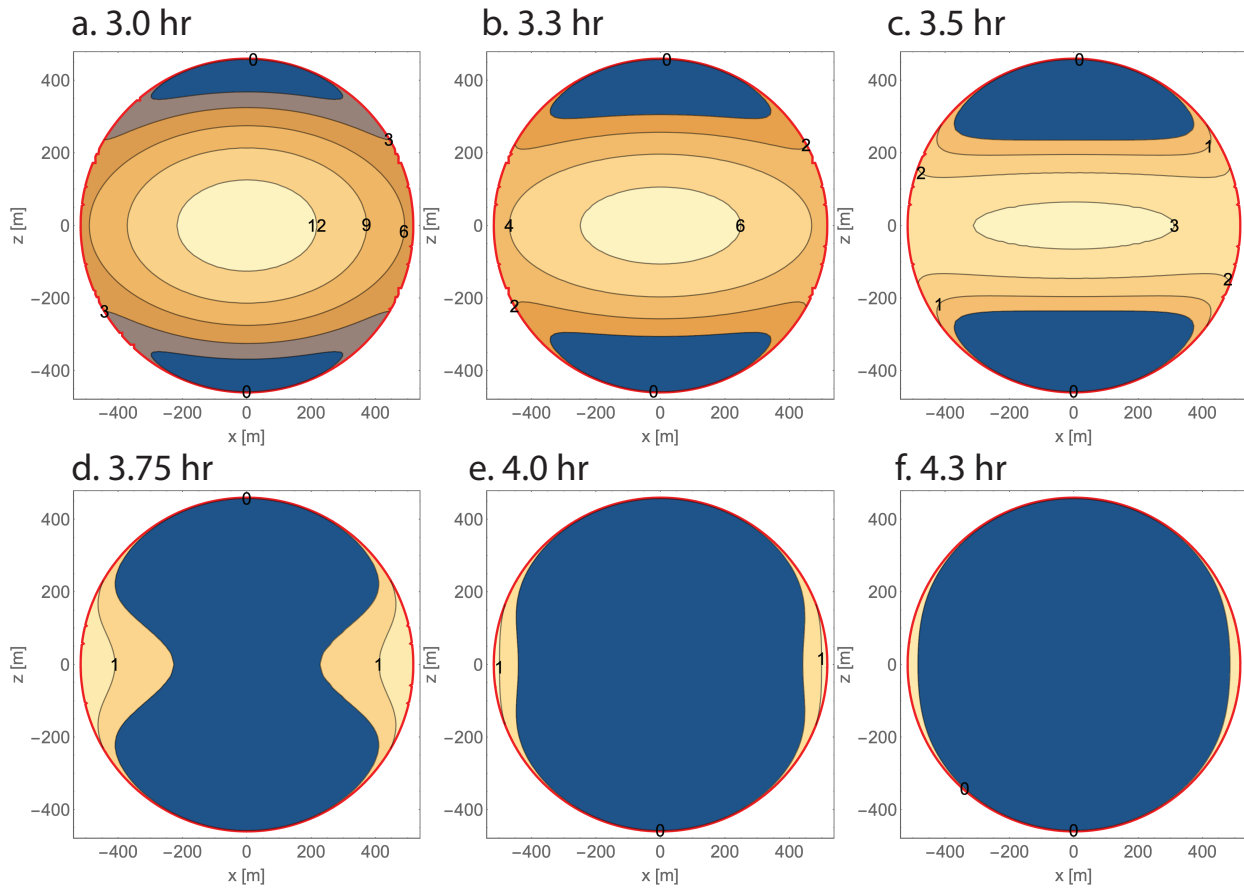


829
 830 *Figure 2. Failed regions of Bennu at different spin periods. The areas in yellow describe*
 831 *structurally failed regions while those in green are intact, given a constant cohesive strength.*
 832 *Panels a and c are the sliced areas along the equatorial regions. Panels b and d show surface*
 833 *regions seen from the spin axes. Panels a and b show the case of the current spin period, 4.3 h,*
 834 *while Panels c and d give a spin period of 3.5 h [Scheeres et al., 2019]. The cohesive strength is*
 835 *fixed at 0.2 Pa for the 4.3 h case and at 0.8 Pa for the 3.5 h case.*
 836



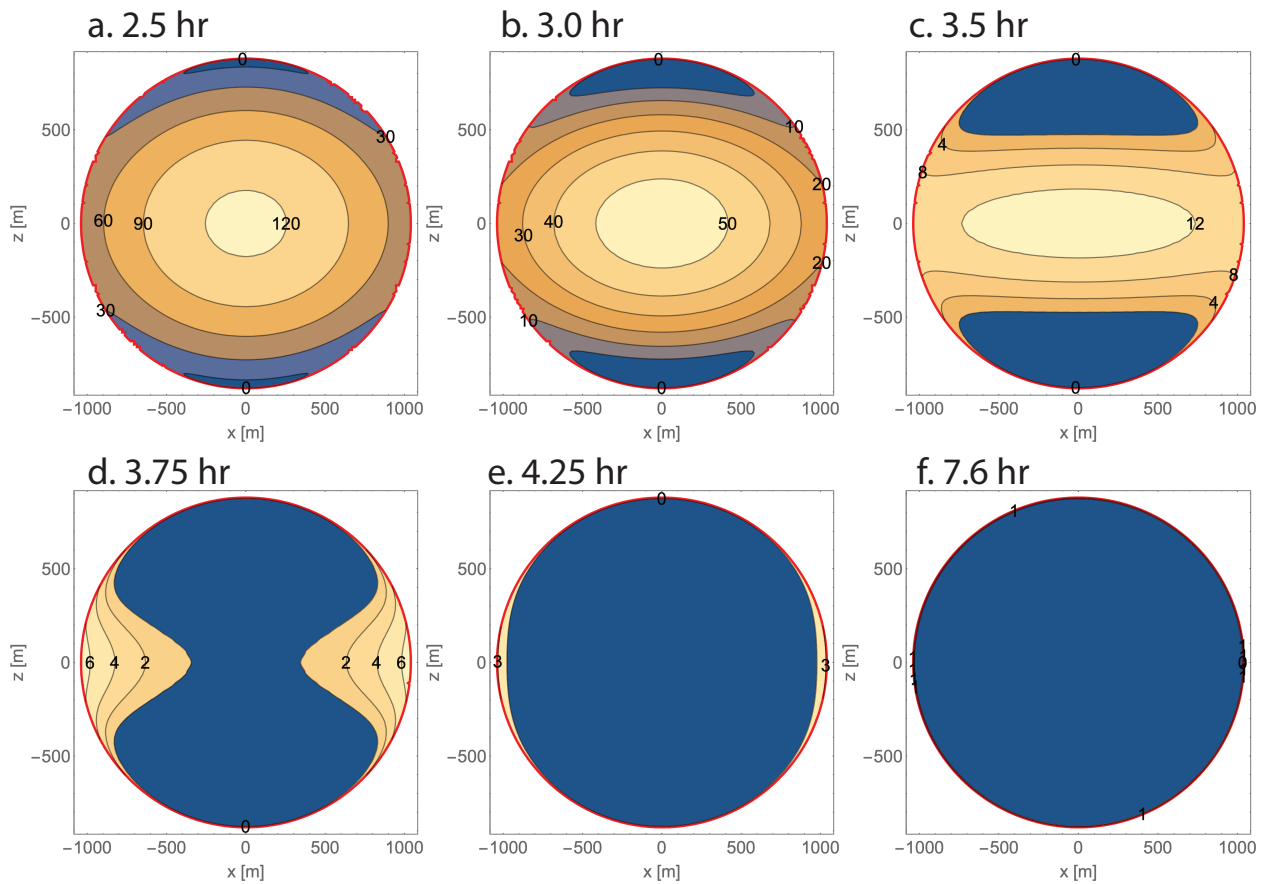
837
 838 *Figure 3. Failed regions of Ryugu at different spin periods, viewed from the spin axis. The*
 839 *format of plot description is the same as in Figure 2. Panels a and b show the case of the current*
 840 *spin period, 7.6 h, while Panels c and d give a spin period of 3.5 h [Hirabayashi et al., 2019;*
 841 *Watanabe et al., 2019]. The cohesive strength is fixed at 1 Pa for the 7.6 h case and at 3.5 Pa*
 842 *for the 3.5 h case.*

843
 844



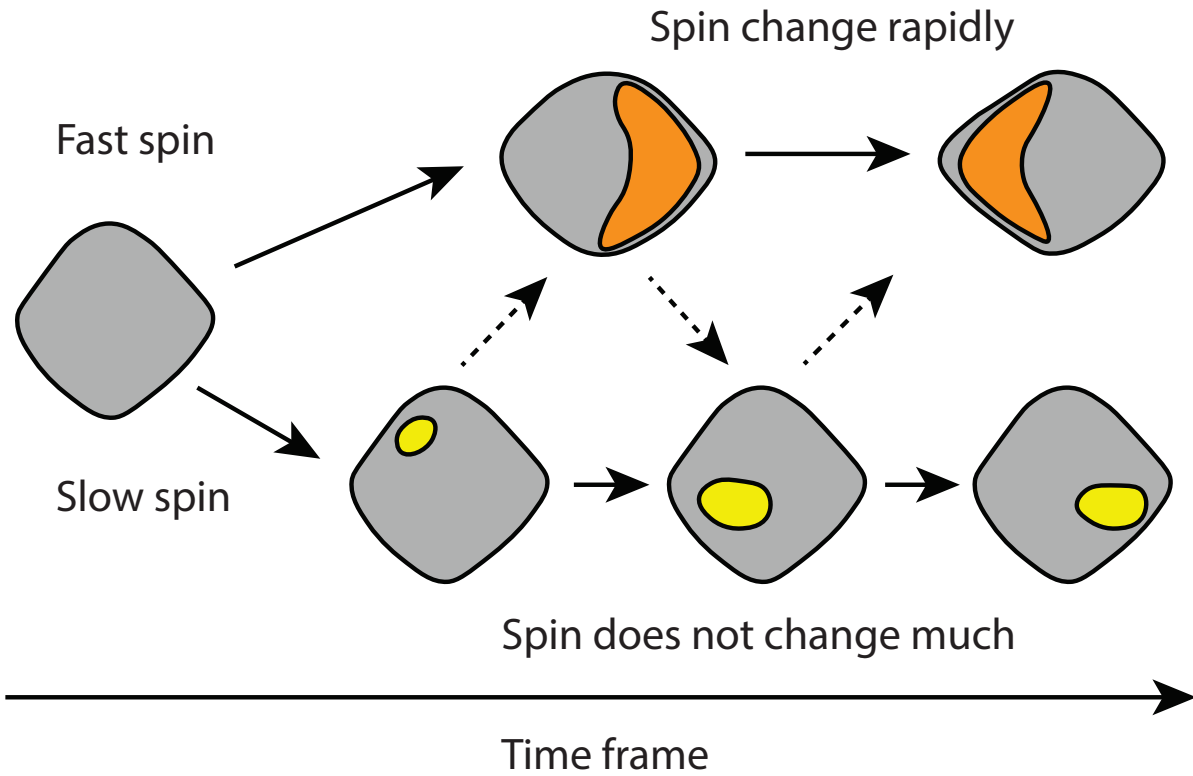
845
 846
 847
 848

Figure 4. Distribution of Y_e^* on the slice along the spin axis of Bennu, derived by the semi-analytical model. The units of the contours are pascals.

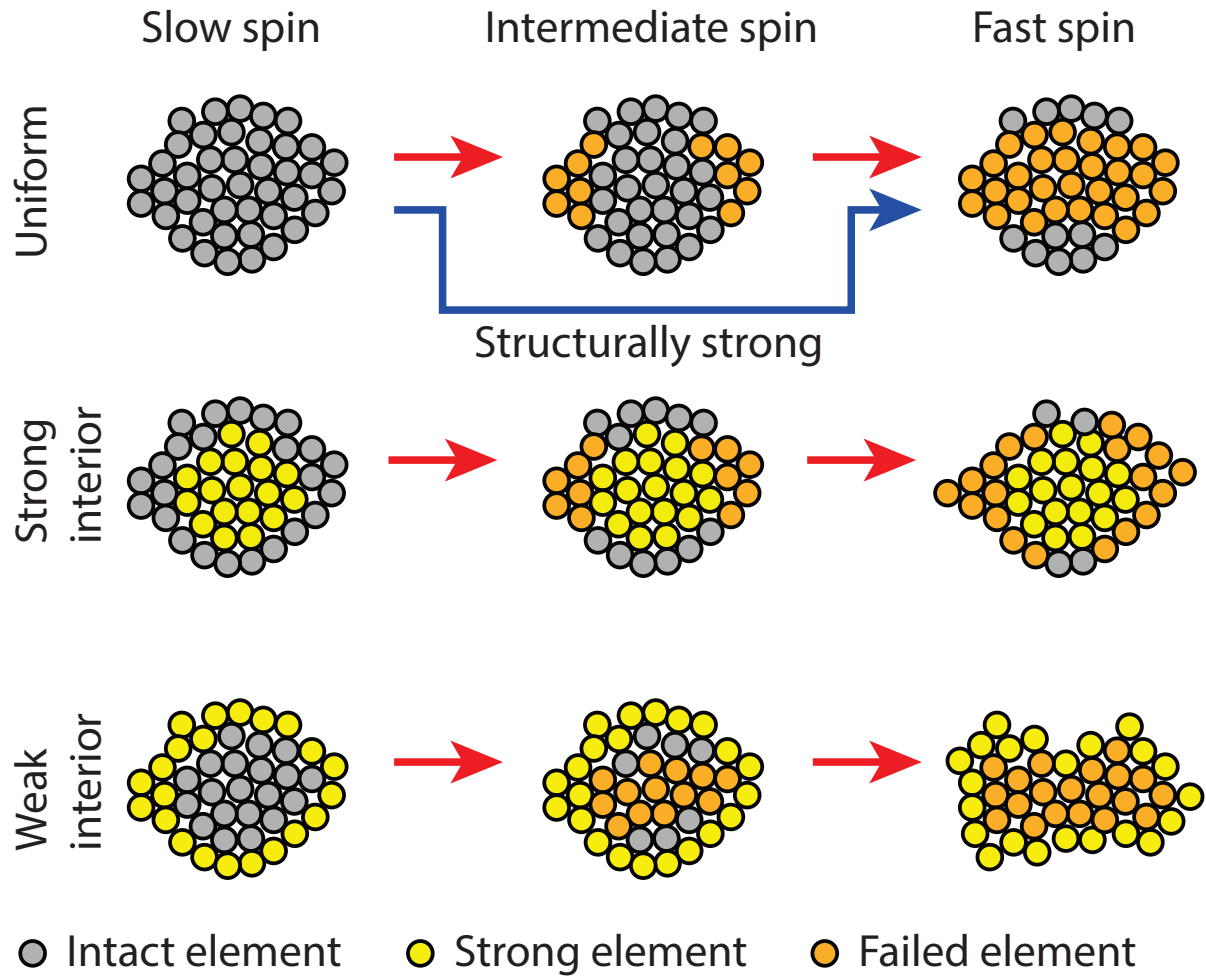


849
 850
 851
 852
 853
 854

Figure 5. Distribution of Y_e^* on the slice along the spin axis of Ryugu, derived by the semi-analytical model. The units of the contours are pascals.



855
 856 *Figure 6. Dependence of failure modes on spin states. The orange patches show large*
 857 *deformation caused by internal failure while the yellow ones describe small surface processes.*
 858 *With fast rotation, a top-shaped body may experience large deformation (the upper path). Slower*
 859 *rotation (but enough for surface failure) can induce small deformation (the lower path).*
 860



861
862
863
864
865

Figure 7. Failure modes that depend on internal structure and spin. This figure is an extended version for the failure mode diagram of a spheroidal asteroid introduced by Hirabayashi [2015]. The case of a weak interior is added based on the study by Sánchez and Scheeres [2018].